Astron. Astrophys. 344, 687–695 (1999)

ASTRONOMY AND ASTROPHYSICS

Temperature predictions for protostellar outflows

J. Hatchell[1], **G.A. Fuller**[1], **and E.F. Ladd**[2]

[1] Department of Physics, UMIST, P.O. Box 88, Manchester M60 1QD, UK
[2] Department of Physics, Bucknell University, Lewisburg, PA 17837, USA

Received 29 September 1998 / Accepted 23 December 1998

Abstract. The acceleration mechanism for protostellar outflows is still uncertain, despite many dynamical studies. Active acceleration processes are expected to heat the molecular gas, and it should be possible to choose between the possible outflow models by excitation studies which measure the temperature of the molecular gas. We show how temperature predictions can be made from a simple bow-shock driven shell model and compared with temperature estimates from excitation studies. As the momentum-conserving shell expands the kinetic energy lost is sufficient to heat the molecular gas to temperatures many times that of the ambient cloud. The energy transfer - and therefore the temperature - is greatest near to the bow shock and therefore the temperature rises with distance from the star. We present a multitransition CO study of the young outflow L483 and compare temperature predictions from the shell model with measurements of the CO excitation.

Key words: ISM: kinematics and dynamics – ISM: jets and outflows – stars: formation – ISM: molecules – ISM: abundances

1. Introduction

All low mass stars are thought to drive massive molecular outflows for some period of their early evolution. Yet the mechanism by which these outflows are generated and driven remains uncertain (eg. review by Bachiller 1996). The process by which the molecular gas is accelerated to the observed outflow velocities is likely also to heat the molecular gas. The observational signature of this heating provides a potential probe of the acceleration mechanism. Using molecular line excitation studies to determine the gas temperature in protostellar outflows can provide a test, in addition to the outflow dynamics, of outflow acceleration models.

Several models for outflows have been put forward. These generally fall into one of two categories: wide-angle winds; and jet-driven outflows. Non-isotropic radial winds may explain both jet and molecular outflow features as different components of the same stellar wind (Shu et al. 1991; Mellema & Frank 1997). Models of jet-driven outflows, on the other hand, assume that the stellar wind originates from close to the star as a highly collimated jet which then entrains molecular material forming the molecular outflow. Momentum can be transferred from the jet to the molecular gas either through shocks or through turbulent mixing along the length of the jet (De Young 1986; Cantó & Raga 1991; Taylor & Raga 1995). Bow shocks can be either at the head of the jet (Masson & Chernin 1993, Chernin & Masson 1995) or at working surfaces within the jet (Raga & Cabrit 1993). Hydrodynamic and magnetohydrodynamic numerical models which contain one or more of these features have been developed (eg. Smith et al. 1997).

Of these, one of the most promising models is the jet-driven bow shock model, which succeeds in explaining both the clumps of shocked H_2 commonly seen at the end of outflows, and the shell structures observed in young sources such as L1157 (Gueth et al. 1996), L1448 (Bachiller et al. 1995) and HH111 (Nagar et al. 1997). Masson & Chernin (1993; hereafter MC93) calculated the dynamics of such a bow-shock driven shell using a simple analytical model. The MC93 model outflows produces features similar to observed CO lobes: sharp velocity peaks behind the bow shock; velocity increasing with distance from the star; shell structures; and high collimation. Although the model predicts a narrow range of velocities at each position, once turbulence and beam dilution are taken into account the observed mass distributions can also be reproduced (MC93).

In this paper we show how predictions for the temperature of the outflow can be made from MC93's shell model, and compare with an observational study of the young outflow in the Lynds dark cloud, L483. Sect. 2 describes the model in detail and displays the predicted temperature distributions. Sect. 3 contains the observational results and the comparison with the model's predictions. We summarize the conclusions in Sect. 4.

2. Predicting temperature in a swept-up shell

In the jet-driven bow shock model, rotational CO transitions trace material that has been swept up behind the bow shock. In the MC93 model this swept-up gas forms an expanding, forward-moving shell in a momentum-conserving 'snow-plough' phase. By considering the dynamics of the shell, we can predict the temperature distribution in the CO outflow.

Following MC93, the shell contains the material swept up from the cavity along its path, and its momentum is determined

Send offprint requests to: J.Hatchell@umist.ac.uk

Table 1. Fundamental parameters of outflow shell model.

Symbol	Parameter	Value
ρ_j	jet density	10^4 cm^{-3} $\times$ $m_{\rm H_2}$
v_j	jet speed	100 km s^{-1}
r_j	jet radius	0.001 pc
ϵ	jet efficiency	1.0
α	angle between shell velocity and jet velocity	20°
ρ_0	ambient density at z_0	$2\,10^4$ cm^{-3} $\times$ $m_{\rm H_2}$
z_0	distance at which ambient number density is ρ_0	0.06 pc
β	density power law index	0,1,2
age	age	$10^{3.2}$, $10^{3.4}$ and $10^{3.8}$ years

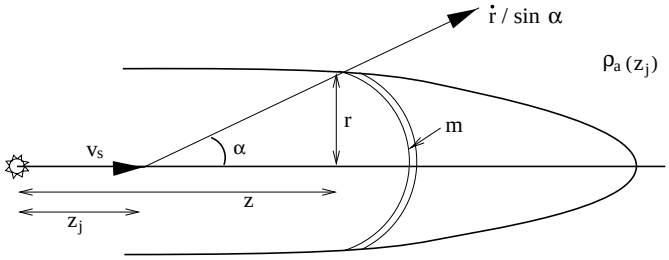

Fig. 1. Shell model geometry, showing the ring of mass m coasting at angle α to the jet axis (after MC93).

by momentum transfer and thermal pressure at the bow shock. The thermal pressure is quickly dissipated close to the jet head and the shell behind the bow shock coasts outwards at a constant angle α to the jet direction (MC93). The shell slows as it continues to sweep up mass from the ambient medium, conserving momentum but losing energy in the form of radiation, in a way analoguous to the later stages of a supernova shell. By considering the energy balance (heating vs. cooling) in the shell, we determine the temperature of the shell.

We now look at the equations that govern the shell in the momentum-conserving phase. All shell quantities are calculated per unit length. The fundamental parameters of the model are given in Table 1. Fig. 1 illustrates the geometry of the model.

The evolution of jet length z_j with jet travel time t_j is found from the shock speed, given by MC93 as

$$v_s = \frac{dz_j}{dt_j} = \frac{\epsilon v_j}{(1+\sqrt{\rho_a(z_j)/\rho_j})}. \qquad \text{(jet length)} \tag{1}$$

where $\rho_a(z_j)$ is the ambient density, ρ_j the jet density, v_j the jet velocity and ϵ the jet efficiency. We assume the power law density distribution

$$\rho_a(z_j) = \rho_0 \left(\frac{z_0}{z_j}\right)^{\beta} \tag{2}$$

where ρ_0 is the density at distance z_0. This is equivalent to a spherically symmetric radial density distribution as the outflow remains narrow $r \lesssim z$. We neglect the ambient density variation during the evolution of each shell section, taking the density equal to that at the point of origin of the section as in MC93. Each coasting shell section travels a distance which is short compared to the total length of the outflow.

The shell mass per unit length is

$$m = \pi r^2 \rho_a + m_0 \qquad \text{(mass)} \tag{3}$$

where r is the shell radius and m_0 is the mass initially injected from the jet.

MC93 neglect m_0, which is justified in their analysis as they consider only light jets which do not contribute much mass. Following measurements of $\rho_j = 10^4$ cm^{-3} in some jets (Bacciotti et al. 1995) we cannot neglect the mass input from the jet. The mass input rate to the shell from the jet equals the mass input from the jet minus the mass used in extending the jet length; per unit length of the shell this is

$$m_0 = \pi r_j^2 \rho_j (v_j/v_s(z_j) - 1) \tag{4}$$

where $v_s(z_j)$ is the rate of advance of the jet head shock at the axis position z_j from which the shell element started.

The momentum equation is

$$p = \frac{m\dot{r}}{\sin\alpha} = p_0 \qquad \text{(momentum)} \tag{5}$$

where the initial momentum p_0 in the direction α is related to the jet parameters by

$$p_0 = \frac{\pi r_j^2 \rho_j v_j}{\epsilon}\left[(1-\epsilon) + \sqrt{\frac{\rho_a}{\rho_j}}\right]\frac{1}{\cos\alpha}. \tag{6}$$

For ϵ close to 1 or $\rho_a \gg \rho_j$ this approximates to the formula given in MC93. We neglect the distance that the shell travels under the power of thermal pressure at the bow shock. This distance is short – the shell is momentum driven within one jet radius of the shock (Chernin et al. 1994; Raga & Cabrit 1993) – and hardly affects the derived outflow shapes.

The kinetic energy of the shell is simply

$$E = \frac{1}{2}\frac{m\dot{r}^2}{\sin^2\alpha}. \qquad \text{(energy)} \tag{7}$$

To form an element of shell we consider that the jet travels to a distance z_j and the shell then propagates outwards at angle α to the jet axis. By solving the jet length equation (Eq. 1) for z_j and then the momentum equation (Eq. 5) for r, the radius r, velocity $\dot{r}$, and energy E of each shell element are found as a function of the jet travel time parameter t_j. The prescription for solving the equations to derive the energy input rate $\dot{E}$ is as follows. Firstly the momentum equation (Eq. 5) must be integrated to give $r(t)$ where t is the shell travel time from its origin at the jet axis. $\dot{r}(t)$ then follows by differentiating. The energy equation (Eq. 7) gives E as a function of $\dot{r}(t)$, and differentiating again gives $\dot{E}(t)$. Next, $z_j(t_j)$ for the progression of the shock is found by solving the jet length differential equation (Eq. 1). In the expression for $\dot{E}(t)$, ρ_a and t are both functions of the on-axis origin of the shell, $z_j(t_j)$ and therefore of t_j: $\rho_a(t_j)$ is given by Eq. 2 upon substitution for z_j, and $t = \text{age} - t_j$ (the shell expansion time at each position is the total age of the outflow

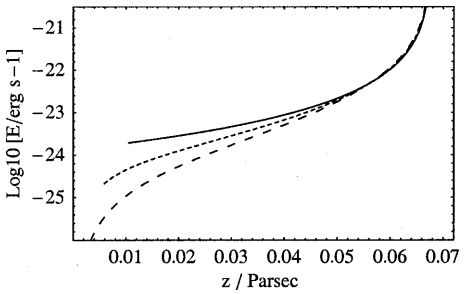

Fig. 2. Energy input rate to each element of the shell, as a function of distance from the source, for outflow parameters given in Sect. 2. The solid, short dashed and long dashed lines correspond to $\beta = 0, 1$ and 2 density distributions, respectively.

minus the time taken by the jet to reach the position on the z-axis from which the shell element was ejected).

We used Mathematica (Wolfram 1996) to solve the equations for $\dot{E}(t_j)$ and the distance from the source $z(t_j) = z_j(t_j) + r(t_j)/\tan\alpha$. These quantities can then can be plotted against each other.

The kinetic energy lost by the shell is radiated away in molecular lines, and the balance between the energy input rate and the line cooling determines the temperature of the shell. Some of the energy may also be lost to turbulence: we consider as limiting cases the equipartition case where thermal and turbulent energies are equal, and also the case where turbulence is negligible and all the energy goes into heating. To convert our energy input rates to temperatures, we use the results of Neufeld et al. (1995). They calculate the cooling rate for molecular gas with temperatures from 10 K upwards and densities above $10^3\,\mathrm{cm}^{-3}$, appropriate for molecular outflows. The temperature which corresponds to a particular energy input rate $\dot{E}$ also varies with shell density n and with an optical depth parameter $\tilde{N}(H_2)$ which corresponds to the column density per unit velocity and determines the radiation transfer through the gas. Both of these parameters also vary along the length of the outflow. We take an average $\tilde{N}(H_2)$ at each position to be the column density divided by the total velocity range. The density n in the shell is not directly predicted by our dynamical model but is constrained to be more than the ambient number density by a factor of (shell volume)/(cavity volume). We take n to be a constant factor of 6 times the ambient density, 6 being the maximum compression possible across a strong shock in molecular gas (Dyson & Williams 1997). Note that the temperature varies only slowly with n: a change from $n = 10^5\,\mathrm{cm}^{-3}$ to $n = 10^6\,\mathrm{cm}^{-3}$ at $\tilde{N} = 10^{21}\,\mathrm{cm}^{-2}\,(\mathrm{km\,s}^{-1})^{-1}$ corresponds to a change of at most 0.2 in $\log_{10} T$.

The fundamental parameters on which the model depends are given in Table 1. The parameters are independent so we cannot reduce their number by forming combinations. As there are nine parameters, it is not possible to explore all reasonable ranges of values in this paper. Instead we pick the values listed in Table 1, which are chosen from the literature to be representative of young outflows, and choose the ages to produce an outflow of the same length as L483 (see observations, Sect. 3) for easy comparison.

All choices of parameters result in energy deposition which increases towards the end of the jet. A rise in temperature with distance from the source is a general result of the bow shock driven shell scenario. This is because the energy input rate depends more heavily on time than on any other parameter, so the young parts of the shell nearer the bow shock have the most energy input and are hotter whereas the old sections near the star have slowed and are cooler.

The values taken for the parameters are as follows. For the jet parameters, jet density $\rho_j = 10^4\,\mathrm{m_{H_2}}$ from optical jet observations (Bacciotti et al. 1995); jet radius $r_j = 0.001$ pc or $1''$ at the L483 distance of 200 pc; jet transfer efficiency $\epsilon = 1$ (MC93); and jet speed $v_j = 100\,\mathrm{km\,s}^{-1}$. For the ambient density, we consider $\beta =$ 0,1 and 2 for constant, $1/z$ and $1/z^2$ density distributions with $\rho_o = 2 \times 10^4\,\mathrm{m_{H_2}}$ at $z_0 = 60''$ (0.06 pc at 200 kpc). The age of the outflow (to get the $70''$ measured length of L483 assuming a plane-of-the-sky inclination and the other parameters as stated) is taken to be $10^{3.2}$, $10^{3.4}$ and $10^{3.8}$ years for $\beta =$ 0,1 and 2 respectively.

Fig. 3 shows the temperature as a function of distance along the outflow for the outflow parameters given above and a $z^{-\beta}$ density distribution with $\beta =$ 0,1 and 2. The temperatures towards the end of the jet are similar regardless of the ambient density distribution, reaching many hundreds of kelvin towards the end of the jet in all cases. The temperatures rise towards the jet head, with the steepest temperature gradient corresponding to the steepest density gradient. For the flat density distribution, temperatures never fall below 60 K. (For a $\beta = 2$ density distribution, temperatures fall unrealistically low near the source, because we have not included the usual ISM heating sources (microwave background radiation, cosmic rays) which would cause the temperatures to level off at ~ 10 K in the inner parts.) Note that the kink in the curves at $\sim 10^{2.5}$ K is due to structure in the cooling rates at around this temperature.

The temperature predictions are plotted up to the bow shock (here 0.067 pc from the source) but the model fails close to the bow shock firstly because the shock speed may be sufficient to dissociate the gas, and the molecular cooling function is then not valid, and secondly, because the outflow is not momentum-conserving. In addition, until sufficient column density has been swept up ($\sim 10^{20}\,\mathrm{cm}^{-2}$), the CO will not be detected. The first shell segment is found a distance $r\tan\alpha$, or between 0.002 and 0.01 pc from the star in our models.

Collisions with dust grains become important for energy transfer at high densities $\gtrsim 10^5\,\mathrm{cm}^{-3}$; these can either cool or heat the gas depending on the temperature of the dust. A full consideration of energy transfer to dust is beyond the scope of our model but we also show in Fig. 3 how a cool (10 K) dust population results in a faster falloff of temperature close to the source where densities are high. The figure illustrates the $\beta = 1$ density distribution case: flatter density distributions with lower central densities are less affected by dust cooling. Fig. 3 shows the lower temperatures which result from assuming half the energy input is lost to turbulence rather than heating, again

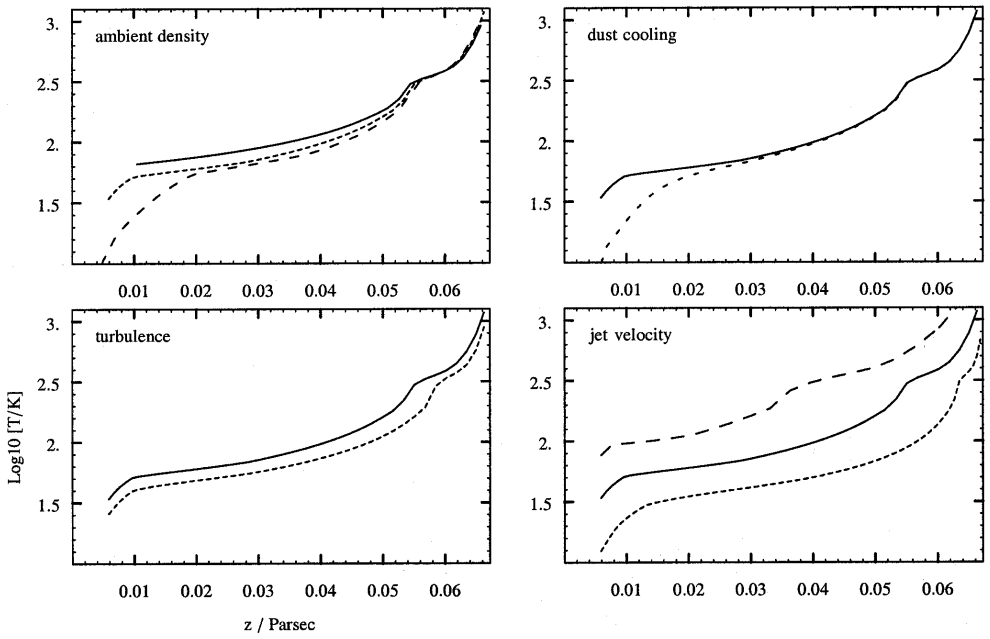

Fig. 3. Temperature of element of the shell, as a function of distance from the source (in parsecs assuming a distance of 200 pc), with (*top left*) $z^{-\beta}$ density distributions with $\beta = 0$ (solid), 1 (short dashed) and 2 (long dashed); (*top right*) a z^{-1} density distribution with (dashed) and without (solid) dust cooling; (*bottom left*) a z^{-1} density distribution with thermal energy only (solid) and thermal/turbulence equipartition (dashed); and (*bottom right*) for a z^{-1} density distribution with jet velocities of 50 km s^{-1} (bottom dashed), 100 km s^{-1} (solid), and 200 km s^{-1} (top dashed). Other outflow parameters are those given in Sect. 2.

for the $\beta = 1$ density distribution. The $\beta = 0$ and 2 density distributions are similarly affected.

General features of these models are that the temperature rises towards the end of the jet, reflecting the increased energy input, and that temperatures mid-outflow are of order 80 K, dropping to a few tens of kelvin close to the source and rising above 500 K within 0.01 pc of the end of the jet.

The model can produce hotter or colder outflows, if the energy input from the jet is increased or decreased. Temperature scales approximately linearly with the jet velocity: Fig. 3 shows the temperature distribution for $\beta = 1$ models calculated with jet velocities $v_j = 50, 100$ and 200 km s^{-1}. Other parameters which affect the energy input in a similar way to v_j are the jet area πr_j^2 and the jet density ρ_j. Increasing the angle between the shell velocity and the jet velocity, α, also has a similar effect to raising v_j. Raising the ambient density produces older, cooler outflows for the same outflow length.

For comparison, both Lizano & Giovanardi (1995) and Cantó & Raga (1991) consider outflow models in which the molecular gas is entrained by mixing at the boundary between a jet/wind and its molecular surroundings. In the entrainment models, the kinetic energy from the wind is input along the whole length of the outflow, rather than being predominantly deposited at the jet head. Entrainment models therefore predict temperatures > 1000 K along the whole length of the jet. Similar temperatures are also reached in the shell model, but only towards the jet head where the jet energy is being deposited (Fig. 3). However, much of the jet energy is radiated at the bow shock rather than providing energy input to the shell, and the shell loses energy rapidly as it ploughs into the surrounding gas.

In addition, both entrainment models predict that the temperature should fall rather than rise towards the end of the outflow. In the Lizano & Giovanardi model, the temperature of the mixing layer rises at first and then falls further from the source. The turnover occurs about 20% along the outflow which they are modelling (L1551). The Cantó & Raga mixing layer temperatures decrease monotonically with distance from the source. This is the opposite gradient to what is predicted by the shell model.

3. An example: L483

To test the temperature model we have carried out a multitransition CO excitation study of the outflow from the young protostellar source IRAS 18148-0440 in the Lynds 483 dark cloud. This bipolar outflow was first detected in ^{12}CO 2–1 by Parker et al. (1991) in a survey of IRAS sources in dark clouds. The outflow is associated with the infrared source IRAS 18148-0440 and a coincident radio source (at RA $= 18^{\rm h}14^{\rm m}50\overset{\rm s}{.}6$ Dec $= -4^\circ 40' 49''$ (B1950); Anglada et al., priv. comm.). The estimated distance to the source is 200 pc. The infrared and radio source is classified as a 'Class 0' source, a young, deeply embedded protostar. The source is centred in a dense core which has been observed in NH_3 and HC_3N, $C^{18}O$ and in the mm and submm continum (Fuller & Myers 1992; Ladd et al. 1991; Fuller & Wooten 1999). The visual extinction along the line of sight to the source is ~ 78 mag.

Fuller et al. (1995) mapped the molecular outflow in ^{12}CO 3–2 at J, H and K infrared bands, and in 2.12 μm molecular hydrogen emission. These observations show the outflow to be compact, bipolar with a high degree of symmetry and highly collimated. The simple structure, along with the identification of the driving source as extremely young make this outflow an excellent candidate for testing outflow models.

The observations consist of a fully-sampled map of the outflow in ^{12}CO 4–3 plus spectra at selected positions in ^{12}CO 2–1 and ^{13}CO 2–1. The $J = 4$–3 transition lies 55 K above ground and the ratio of this line to lower energy transitions can be sensitive to temperatures up to ~ 100 K. We use the line ratios

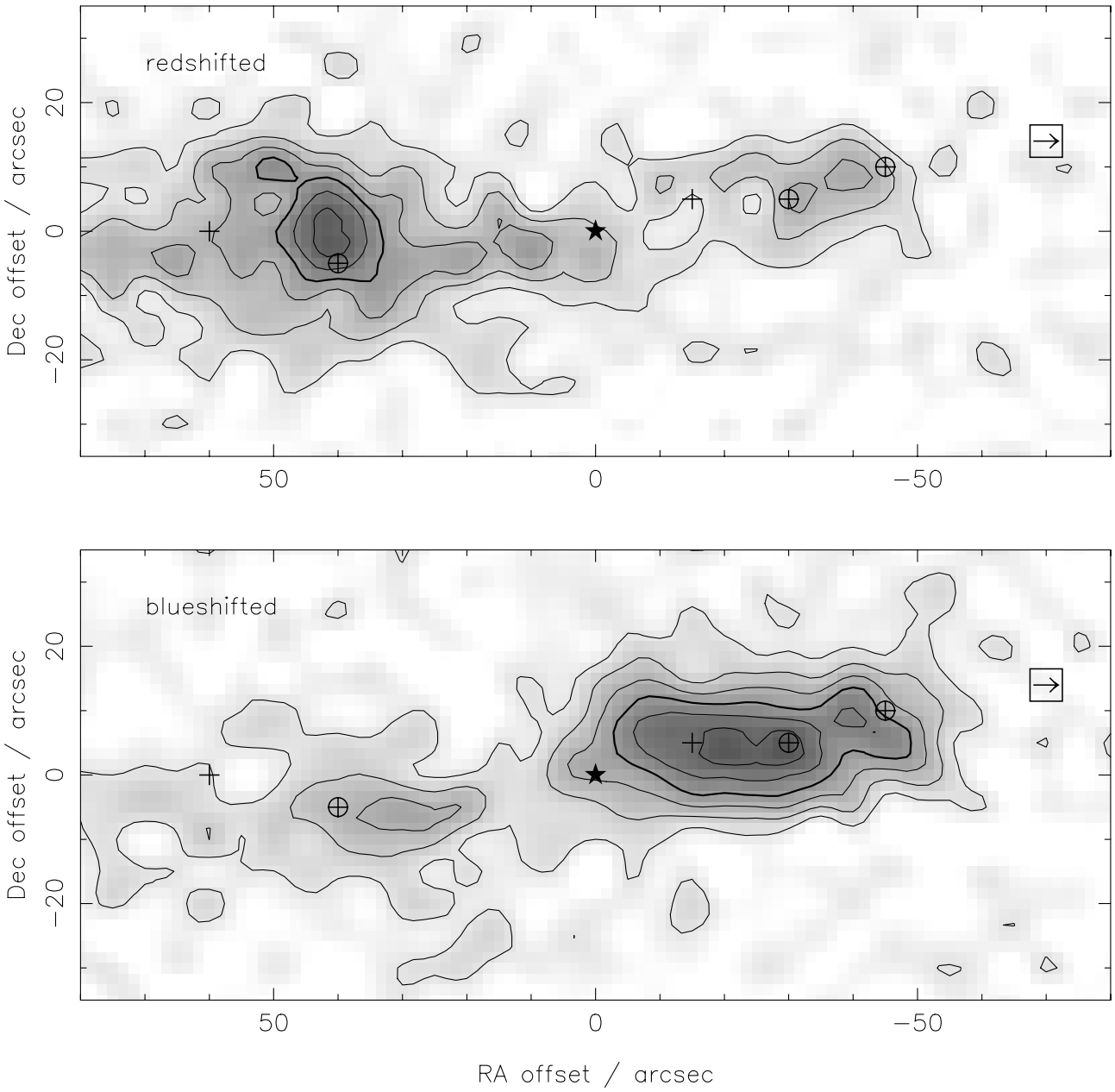

Fig. 4. Integrated intensity maps of ^{12}CO 4–3. Redshifted emission (*top*) is integrated from 5.5 to 15.5 km s^{-1} and blueshifted (*bottom*) from -4.5 to 5.5 km s^{-1}. Contours are every 10 K km s^{-1} from 10 K km s^{-1}. The position of the VLA source is marked with a star. Positions at which ^{12}CO 2–1 spectra were taken are marked with crosses, and positions where ^{13}CO spectra were taken with circles. There is strong H_2 emission at the position marked with the square and arrow, which may mark the jet head. Offsets are (RA, Dec) in arcseconds from RA $= 18^{\rm h}14^{\rm m}50\overset{\rm s}{.}6$ Dec $= -4^\circ40'49''$ (B1950). Note that the coordinates of the H_2 emission have changed substantially from that shown in Fuller et al. 1995: the coordinates were checked during the 1997 observations and are now correct to within $1''$.

to constrain the temperature at several positions in the outflow,compare the results with the shell heating predictions of Sect. 2, and look for any temperature gradients along the outflow lobes, which might differentiate between outflow acceleration models.

The observations were taken at the James Clerk Maxwell Telescope (JCMT) during July 1996, May 1997 and August 1998 using the common user heterodyne receivers A2 and C2. Transitions and observing parameters are given in Table 2. Positions observed in each transition are given in Table 3. All spectra are corrected for the forward scattering and spillover efficiency $\eta_{\rm fss}$ to give $T_{\rm R}^*$ in kelvin. We position switched to cancel sky emission using an off position of ($600''$, $200''$) in 1996 and 1997 and ($0''$,$1800''$) in 1998. We checked these off positions for emission in ^{12}CO 2–1 by comparing with a number of other positions: ($600''$,$200''$) showed a small amount of emission between 2 and 7 km s^{-1} with a line brightness of up to 2 K; this was less at ($0''$,$1800''$) (the systemic velocity of L483

Table 2. Observing parameters in L483: frequency, beam FWHM, efficiency, typical system temperature, bandwidth and integration time.

	^{12}CO 4–3	^{12}CO 2–1	^{13}CO 2–1
ν(GHz)	461.041	230.538	220.399
$\theta_{\rm B}$ ($''$)	11	21	22
$\eta_{\rm fss}$	0.7	0.8	0.8
$T_{\rm sys}$(K)	2060	380	340
$\Delta\nu$ (MHz)	125	250	125
$t_{\rm int}$ (s)	4	120	1200

Table 3. Positions observed in L483. Offsets are (RA, Dec) in arcseconds from RA $= 18^{\rm h}14^{\rm m}50\overset{\rm s}{.}6$ Dec $= -4^\circ40'49''$ (B1950).

Line	positions
^{12}CO 4–3	map $160'' \times 70''$ at $5''$spacing.
^{12}CO 2–1	(60,0)
	(40,-5)
	(0,0)
	(-15,5)
	(-30,5)
	(-45,10)
^{13}CO 2–1	(40,-5)
	(-30, 5)
	(-45,10)

is 5.5 km s^{-1}. In ^{12}CO 4–3 we made an 'on-the-fly' raster map, in which the telescope scanned in right ascension at succesive declinations, storing the result every $5''$ to build up a map of the source (Fig. 4).

Fig. 4 shows the positions at which we observed ^{12}CO 2–1 and ^{13}CO 2–1 in addition to ^{12}CO 4–3. Fig. 4 also shows that both outflow lobes show evidence for redshifted and blueshifted gas, suggesting an inclination close to the plane of the sky. We refer to the lobe at negative RA offset, which shows the strongest blueshifted emission, as the blue lobe, and the lobe at positive RA offset as the red lobe.

3.1. Temperature measurements from CO ratios

To estimate the gas temperature from the CO observations we use the ^{12}CO $J = 4$–3 line as a high excitation line, $J = 2$–1 as a low excitation line, and ^{13}CO $J = 2$–1 to determine the optical depth in the ^{12}CO. ^{13}CO is less abundant than ^{12}CO and we take it to be optically thin in outflows. The ^{12}CO/^{13}CO ratio gives the optical depth in ^{12}CO. The CO 4–3/CO 2–1 ratio gives the excitation temperature $T_{\rm ex}$. This is a good estimate of the kinetic temperature $T_{\rm k}$ if the gas density is above the critical density of the higher energy transition, 2×10^4 cm^{-3} for $J = 4$–3. We assume $T_{\rm ex} = T_{\rm k}$ throughout.

First we find the excitation temperature from the ^{12}CO 4–3/^{12}CO 2–1 line ratio. Differences in beam filling factors between the CO $J = 4$–3 and $J = 2$–1 observations are taken into account by convolving the maps of the higher resolution transition to the lower resolution beam. This eliminates the beam filling factor from the equations. The excitation temperature which corresponds to a particular line ratio depends on the optical depth as shown in Fig. 5, calculated under the LTE assumption.

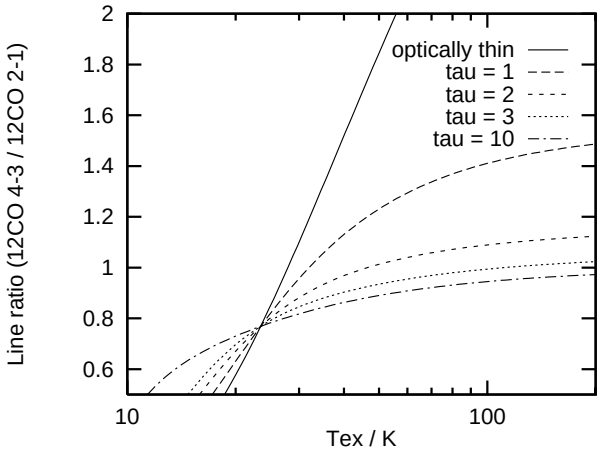

Fig. 5. $T^*_{\rm R}(^{12}$CO 4–3)/$T^*_{\rm R}(^{12}$CO 2–1) as a function of τ_{2-1} for various $T_{\rm ex}$.

The optically thin limit ($\tau << 1$), shown as a solid line on the graph, gives lower limits on the excitation temperatures for a given line ratio. For higher optical depths the line ratio becomes less sensitive to temperature, and must be more accurately known to find the temperature.

Spectra extracted from the interpolated ^{12}CO 4–3 map are overlaid on ^{12}CO 2–1 spectra in Fig. 6. Ratio spectra of the ^{12}CO 4–3/^{12}CO 2–1 ratio are also shown in Fig. 6. The ratios are well determined in both red and blueshifted components of each spectrum out to velocities of a few km s^{-1} from ambient.

The 4–3/2–1 line ratios in the dominant wings (blueshifted gas in the blue lobe and redshifted gas in the red lobe) are typically ~ 1.2. The ratios are similar at different positions within the outflow, with the range in the ratio (~ 0.9–1.8) due to scatter rather than to obvious velocity trends. In the optically thin limit, line ratios of 0.9 and 1.8 correspond to temperatures of 26 and 48 K, respectively. Such temperatures are much less than our outflow shell model predicts, particularly at (-45$''$,10$''$) which is only 0.025 pc from the end of the outflow.

The range in ratios is sensitive to the relative calibration of the CO 4–3 and 2–1 bands, a source of uncertainty which could push the ratios up or down by as much as 20%, resulting in correspondingly higher or lower temperatures. However, even for a 20% increase in ratios, the temperature range rises to only 33–48 K, in the optically thin lower limit, still lower than the shell model predicts for the outer parts of the outflow.

However, the same line ratios correspond to much higher temperatures if the optical depth is significant, as indicated in Fig. 5. If the ^{12}CO 2–1 optical depth is significant, of order 2 or more, then even a ratio as low as 0.9 could correspond to a temperature > 100 K once the 20% calibration uncertainty is taken into account. Only if the optical depth is much less than 1 can the temperatures be as low as the lower limits suggest.

We can estimate the ^{12}CO 2–1 optical depth in the usual way from the ^{12}CO 2–1/^{13}CO 2–1 ratio. Assuming that the ^{13}CO

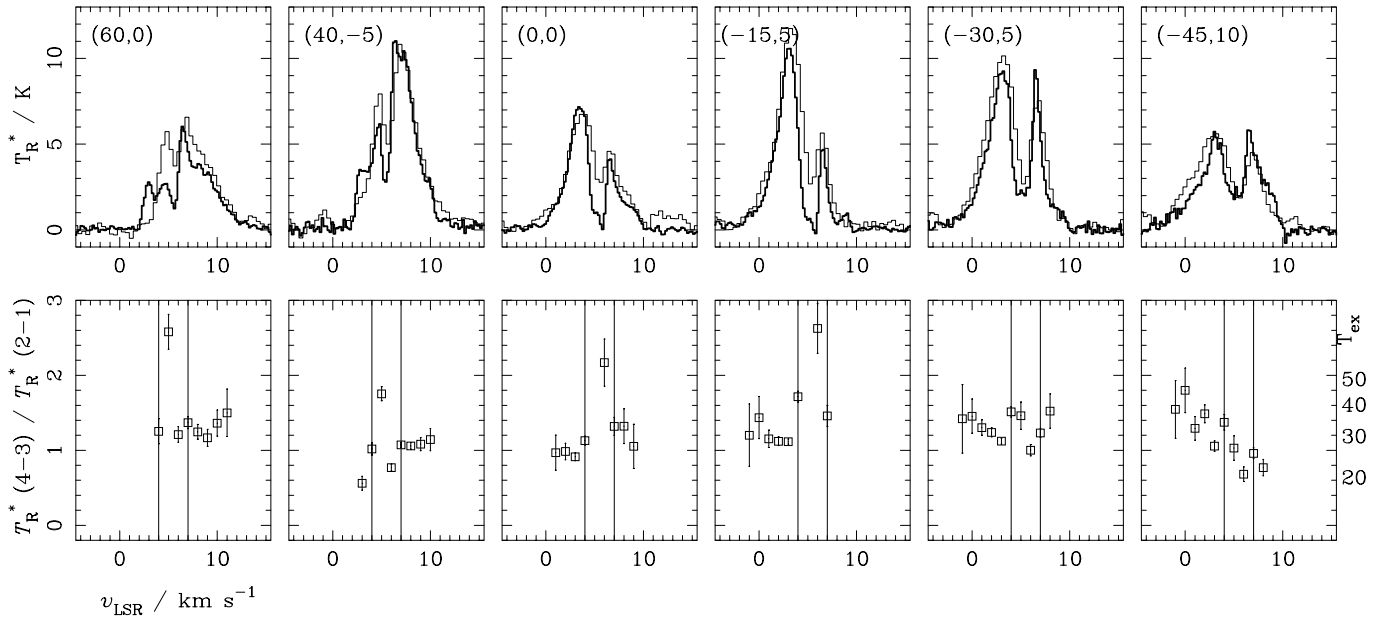

Fig. 6. *Top:* ^{12}CO 4–3 (light) spectra interpolated to a 21″beam overlaid on ^{12}CO 2–1 spectra (heavy) at selected positions. *Bottom:* 4–3/2–1 quotients. Corresponding temperature lower limits are given on the right hand side of the plot, assuming optically thin emission. Errorbars are 1σ and do not include the systematic 20% calibration uncertainty between frequency bands. The vertical lines mark the extent of emission from the ambient cloud.

line is optically thin, and that the ^{12}CO and ^{13}CO have similar beam filling factors (as the beamsizes are similar) and the same excitation temperature, the ratio of the brightness temperatures is given by

$$\frac{T_{\rm R}^*(^{12}{\rm CO})}{T_{\rm R}^*(^{13}{\rm CO})} = \left(\frac{\nu_{12}}{\nu_{13}}\right)^2 \frac{[^{12}{\rm C}]}{[^{13}{\rm C}]} \frac{(1-e^{-\tau_{12}})}{\tau_{12}} \quad (8)$$

where subscripts of 12 and 13 indicate ^{12}CO and ^{13}CO transitions of the same J, respectively. Wilson & Rood (1994) derive a mean value of 77, and Langer (1997) gives 67 for $[^{12}{\rm C}]/[^{13}{\rm C}]$ in the local interstellar medium: we assume an average value of 72 in our calculation of τ_{2-1}.

Fig. 7 shows the ^{13}CO 2–1 spectra at (40″, -5″),(−30″, 5″) and (−45″,10″) overlaid with the ^{12}CO 2–1 spectra at the same positions but with the line intensities divided by 30, and the resulting optical depth $\tau(^{12}{\rm CO}\ 2\text{–}1)$ as a function of velocity. The ^{12}CO/^{13}CO ratio is small in the velocity range of emission from the ambient cloud, 4–7 km s^{-1}, and increases to values of 20–40 in the inner line wings. The ratio remains fairly constant over the whole range of velocities, suggesting that outside 4–7 km s^{-1} the ratios are little affected by ambient cloud contamination, as this would raise τ at lower velocities.

It is clear from Fig. 7 that τ_{2-1} is significantly greater than 1 in the inner line wings at all three positions. At low velocities, therefore, we do measure the significant optical depths that are required to reconcile the high temperatures predicted by the shell model with the measured 4–3/2–1 ratios. For $\tau_{2-1} \gtrsim 1$, the temperature lower limits for 4–3/2–1 ratios of 1.0 and 1.5 rise to 33 and 150 K, respectively. These temperatures are much more in line with what is expected from the shell model (Fig. 3). Most of the mass in the outflow is at these low velocities, as can be seen from the ^{12}CO 4–3 spectra (Fig. 6) which are insensitive to cold quiescent cloud material, so it is relatively unimportant that at higher velocities the uncertainties due to noise on the ^{13}CO spectrum are too great for τ_{2-1} to be usefully determined. The temperature estimates rise further for the higher τ_{2-1} measured at some positions and velocities.

Unfortunately, with $\tau_{2-1} \gtrsim 1$, the measured CO 4–3/CO2–1 line ratios do not place strong constraints on the temperature. The 20% calibration uncertainty between bands is a significant source of uncertainty in the temperature determination, as the

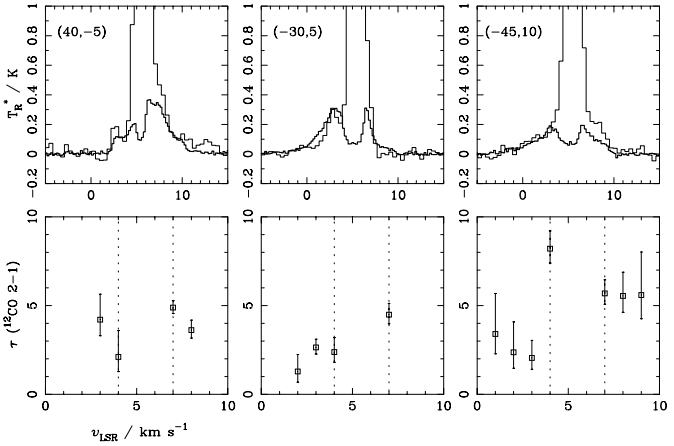

Fig. 7. Top: $T_{\rm R}^*(^{13}{\rm CO}\ 2\text{–}1)$ (light) spectra overlaid with $T_{\rm R}^*(^{12}{\rm CO}\ 2\text{–}1)$ spectra divided by 30 (heavy). Bottom: $\tau(^{12}{\rm CO}\ 2\text{–}1)$ calculated from the ^{12}CO/^{13}CO ratio. Errorbars are $1-\sigma$. Note the different velocity scales. The vertical lines mark the extent of emission from the ambient cloud.

4–3/2–1 ratio becomes less sensitive to temperature at higher optical depths (Fig. 5).

3.2. Evidence for temperature gradients?

Returning to the 4–3/2–1 line ratios, is there any evidence for temperature gradients along the outflow lobes, which might differentiate between outflow acceleration models? In fact the 4–3/2–1 ratios are similar at the different positions along the lobes, with possibly a slight rise towards the end of the blue lobe. In addition, comparing the positions ($-30''$,$5''$) and ($-45''$,$10''$) in the blue lobe (Fig. 7), the optical depths are also similar. This suggests that temperatures do not change by much along the length of the outflow.

The shell model predicts that the temperature should rise and the optical depth drop towards the end of the outflow. The temperatures rise towards the end of the jet because this is where the energy input is greatest, but the optical depth falls because further out from the star the shell has swept up less mass, particularly if the density gradient is steep. (The shell column density largely reflects the ambient density distribution). Therefore, for steep density gradients, the shell model predicts that the 4–3/2–1 ratios should increase steeply towards the end of the outflow. In the shell model, only shallow density gradients can produce the similar or slightly rising 4–3/2–1 ratios observed in L483.

A shallow density gradient in the outer half of the outflow is consistent with observations of the environment of L483. The central source is embedded in a high density ridge which is at $\sim 45^\circ$ to the outflow axis. In the central 0.02 pc around the star, the density falls at least as steeply as $z^{-1.5}$ but at larger radii in the outflow direction, the distribution flattens out (Fuller et al. 1995; Fuller & Wooten 1999). Buckle et al. (1999) show that the infrared extinction drops by a factor of 3 between a position 0.015 pc from the star and a position midway along the jet but then stays roughly constant up to the bow shock, again indicating that the steep power law gives way to a more flat density distribution further from the star.

Alternatively, mixing layer models predict decreasing optical depth combined with decreasing temperature, as more gas is swept up near the star and heated to hotter temperatures. These conditions could also produce constant or slightly rising 4–3/2–1 ratios, if the optical depth falls slowly with distance from the star. However, there is no evidence for falling optical depth between the two positions observed in the blue lobe. It may be possible to reconcile some of the highest observed line ratios with the extreme temperatures (> 1000 K) predicted by the mixing layer models, if filling factors are very small. But it is hard to see how enough CO can be entrained to produce the observed column densities in these low-J transitions, given that only small fractions of the CO population would be in the low-J states (1% in $J = 2$ at 1000 K). Unrealistically high ambient densities of $> 10^6\,\mathrm{cm}^{-2}$ more than 0.05 pc from the source would be required to produce an optical depth of 1 in $J = 2$–1, given that the outflow is only a few arcseconds (a few $\times 0.001$ pc) wide and the mixing layer material is assumed to originate from the ambient cloud.

In order to test the temperature predictions of the shell model further, we need to find better temperature probes than optically thick ^{12}CO lines, and observe transitions which trace material from a few tens to a few hundred kelvin. Ratios of optically thin high-J ^{13}CO lines would be useful in this respect. Unfortunately, point-by-point mapping of weak transitions in the submillimetre is too time consuming to be feasible with current single dish telescopes, and current interferometers are not sensitive enough and lack capability at higher frequencies. The large collecting area proposed for the next generation of millimetre interferometers is needed to achieve sufficient sensitivity to map optically thin high excitation transitions at high resolution on reasonable timescales. Array receivers on single-dish telescopes may also speed up data collection times. In addition, IR observations of higher excitation CO lines, such as those carried out with ISO (Liseau et al. 1996), provide strong constraints on average outflow temperatures although with satellite instruments the resolution is too low to study the gradients in any detail. In the meantime, it would be valuable to observe outflows which propagate into low ambient densities and have smaller optical depths in ^{12}CO, as the ^{12}CO 4–3/2–1 ratio is sensitive to temperature in the optically thin case.

4. Conclusions

We have used MC93's bow shock driven shell model of a protostellar outflow combined with molecular cooling rates to predict temperature as a function of length along the molecular outflow. We have compared the results of modelling with observations of the L483 outflow, where we have carried out a multitransition study of CO in order to measure the gas temperature for comparison with the predictions.

In a simple bow shock model, the expanding shell sweeps up the ambient medium, conserving momentum but losing kinetic energy which is available to heat the gas in the shell. By modelling this process we find that the temperature rises with distance from the star towards the head of the driving jet, rising more strongly if there is a falling density gradient away from the star. Comparing the gain in thermal energy with molecular cooling functions, the heating is sufficient to maintain the outflow at temperatures several times hotter than the ambient interstellar cloud for most of its length. For our example model, for which we have chosen parameters typical of young outflows such as L483, the temperature remains over 50 K for at least half the length of the outflow (more if the density gradient is less steep than z^{-2}).

The results of an excitation study of CO in L483 (including transitions up to $J = 4$–3) are consistent with the temperatures and gradients predicted by the shell model, provided the optical depth remains high along the length of the outflow and the ambient density is fairly flat.

Acknowledgements. The authors would like to thank the JCMT staff for their support during the observations, particularly Iain Coulson for general help and for service observation support; also the referee M. Hogerheijde for constructive comments, and an anonymous referee for suggestions based on an earlier version of this paper. This research was

supported by the UK Particle Physics and Astronomy Research Council (PPARC) grant to UMIST. The James Clerk Maxwell Telescope is operated by The Joint Astronomy Centre on behalf of the Particle Physics and Astronomy Research Council of the United Kingdom, the Netherlands Organisation for Scientific Research, and the National Research Council of Canada.

References

Bacciotti F., Chiuderi C., Oliva E., 1995, A&A 296, 185
Bachiller R., 1996, ARA&A 34, 111
Bachiller R., Guilloteau S., Dutrey A., Planesas P., Martin-Pintado J., 1995, A&A 173, 324
Buckle J., Hatchell J., Fuller G.A., 1999, A&A submitted
Cantó J., Raga A.C., 1991, ApJ 372, 646
Chernin L.M., Masson C.R., 1995, ApJ 455, 182
Chernin L., Masson C., Gouveia dal Pino E.M., Benz W., 1994, ApJ 426, 204
De Young D.S., 1986, ApJ 307, 62
Dyson J.E., Williams D.A., 1997, The Physics of the Interstellar Medium. IoP, p. 102, 111, 158
Fuller G.A., Myers P.C., 1992, ApJ 384, 523
Fuller G.A., Wootten A., 1999, in preparation
Fuller G.A., Lada E.A., Masson C.R., Myers P.C., 1995, ApJ 453, 754
Gueth F., Guilloteau S., Bachiller R., 1996, A&A 307, 891
Ladd E.F., Adams F.C., Fuller G.A., et al., 1991, ApJ 382, 555
Langer W.B., 1997, In: Latter W.B., et al. (eds.) CO: Twenty-Five Years of Millimetre-Wave Spectroscopy. IAU, p. 98
Liseau R., Ceccarelli C., Larsson B., et al., 1996, A&A 315, 181L
Lizano S., Giovanardi C., 1995, ApJ 447, 742
Masson C.R., Chernin L.M., 1993, ApJ 414, 230
Mellema G., Frank A., 1997, MNRAS 292, 795
Nagar N.M., Vogel S.N., Stone J.M., Ostriker E.C., 1997, ApJ 482, L195
Neufeld D.A., Lepp S., Melnick G.J., 1995, ApJS 100, 132
Parker N.D., Padman R., Scott P.F., 1991, MNRAS 252, 442
Raga A., Cabrit S., 1993, A&A 278, 267
Shu F.H., Ruden S.P., Lada C.J., Lizano S., 1991, ApJ 370, L31
Smith M.D., Suttner G., Yorke H.W., 1997, A&A 323, 223
Taylor S.D., Raga A.C., 1995, A&A 296, 823
Wilson T.L., Rood R.T., 1994, ARA&A 32, 191
Wolfram S., 1996, The Mathematica Book. 3rd ed., Cambridge University Press